

Hard templating synthesis of mesoporous and nanowire SnO₂ lithium battery anode materials†

Hyesun Kim‡ and Jaephil Cho‡*

Received 27th September 2007, Accepted 17th December 2007

First published as an Advance Article on the web 8th January 2008

DOI: 10.1039/b714904b

Mesoporous and nanowire SnO₂ anode materials for lithium batteries were prepared using KIT-6 and SBA-15 SiO₂ templates, and their electrochemical properties were compared at different current rates. The as-prepared SnO₂ nanowires had a diameter of 6 nm and a length of >3 μm and Brunauer–Emmett–Teller (BET) surface area of 80 m² g⁻¹ while mesoporous SnO₂ showed a pore size of 3.8 nm and a BET surface area of 160 m² g⁻¹. The charge capacities of these two anodes were similar to each other at 800 mAh g⁻¹, but mesoporous SnO₂ showed much improved cycle life performance and rate capabilities because of its higher surface area than nanowire SnO₂. Especially, the capacity retention of the mesoporous SnO₂ was 98%, compared with 31% for the SnO₂ nanowires at a 10 C rate (= 4000 mA g⁻¹). The improved electrochemical performance of the mesoporous SnO₂ was related to the regular porosity which permitted thorough flooding of the electrolyte between the particles, and the mesopores which acted as a buffer zone during the volume contraction and expansion of Sn.

Introduction

Due to the fact that SnO₂ is an n-type semiconductor with a wide band gap ($E_g = 3.6$ eV), it has been intensively investigated in the areas of gas sensors, solar cells, and catalysts.^{1–4} Furthermore, it has been investigated as an anode material for lithium batteries due to its high capacity (>600 mAh g⁻¹) compared with graphite (372 mAh g⁻¹).^{5–8} However, similar to all other lithium reactive materials, it showed a volume change that was greater than 200% during the lithium alloy/dealloy process. This causes cracking and crumbling, resulting in electrical disconnection from the copper current collector. Eventually, rapid capacity fading occurs. In order to minimize such a drastic volume change, morphology controls of SnO₂ by a synthetic method, involving nanotubes,⁹ hollow structures,¹⁰ nanowires,¹¹ mesopores,¹² and nanorods¹³ have been reported. Hollow and nanowire SnO₂ showed improved capacity retention, compared with the bulk analogues. On the other hand, when the bulk particles contain ordered mesopores, these pores act as a buffer layer for volume changes of the pore wall; indeed, mesoporous and crystalline tin phosphate composites showed excellent capacity retention, demonstrating another means of controlling the volume expansion/contraction.¹⁴ However, bulk particles that contain pure mesoporous phase are most ideal for lithium reactive materials.

Recently, Ryoo's group reported the preparation of ordered mesoporous carbon using highly ordered mesoporous silica.¹⁵ After an annealing process, the parent silica materials could be removed selectively. Using this hard template method, CeO₂,¹⁶

Co₃O₄,¹⁷ and M_xO_y¹⁸ were reported. These framework compositions should be stable under the conditions used to dissolve the mold, that is, stable in relatively concentrated NaOH or HF in the case of silica. This method is highly reproducible, and can make use of silica templates. Two types of ordered mesoporous silica were employed as hard templates. A hexagonal SBA-15 silica template with *p6mm* symmetry was used for the template. It contains two-dimensional parallel cylindrical pores arranged with hexagonal symmetry. On the other hand, a three-dimensional KIT-6 silica template had cubic *Ia3d* symmetry. These two pore structures yield nanowire and mesoporous morphologies, respectively.¹⁹

To date, several preparative approaches utilizing a supra-molecular templating mechanism have been reported for the preparation of mesoporous tin oxide.^{12,20} Upon removal of the surfactant, however, the mesoporous structure was destroyed or was somewhat disordered. Moreover, direct synthesis of these types of mesoporous materials using surfactants is often difficult; compared with silica, the surfactant/oxide composite precursors are often more susceptible to a lack of condensation, redox reactions or phase transitions accompanied by thermal breakdown of the structural integrity.¹⁶

In this study, the synthesis and electrochemical properties of mesoporous and nanowire SnO₂ via a hard template method using SBA-15 and KIT-6 silica are reported for the first time. Even after removing the templates, the nanostructured morphologies are maintained. These materials show excellent capacity retention and rate capability levels at higher C rates.

Experimental

Synthesis of SAB-15 and KIT-6 templates

The hexagonal SBA-15 silica and cubic KIT-6 templates were prepared in an aqueous solution using Pluronic 123 (EO₂₀PO₇₀EO₂₀,

Department of Applied Chemistry, Kumoh National Institute of Technology, Gumi, 730-701, Korea. E-mail: jpcho@kumoh.ac.kr

† Electronic supplementary information (ESI) available: Low-angle XRD patterns, N₂ isotherms, pore size distributions and SEM image. See DOI: 10.1039/b714904b

‡ Current address: Department of Applied Chemistry, Hanyang University, Ansan, 426-791, South Korea. E-mail: jpcho123@naver.com

MW = 5800, Aldrich) according to previously reported methods¹⁵ that were modified. To prepare KIT-6, 30 g of P123 was dissolved in 500 g of distilled water and 56 g of conc. HCl (30%). To this solution, 30 g of butanol (Aldrich, 99.9%) was slowly added under stirring at 40 °C. After 2 h stirring, 37 g of tetraethoxysilane (TEOS; Aldrich, 98%) was added at 40 °C. The mixture was left under stirring for 24 h at 40 °C followed by a hydrothermal treatment at 100 °C for 24 h. For the preparation of SBA-15, 30 g of P123 and 30 g of n-butanol (Aldrich, 99.9%) were dissolved in 2000 g of distilled water and 60 g of 30 wt% HCl solution under stirring at 40 °C. TEOS (30 g) was added into the mixed solution at 40 °C under stirring, and the remainder of the synthesis was identical to that of SBA-15. The difference in solvent concentration resulted in a different template structure.

Synthesis of nanowire and mesoporous SnO₂

Cubic *Ia3d* and hexagonal *p6mm* silicas calcined at 550 °C for 3 h were used to prepare mesostructured and nanowire SnO₂. SnCl₄·5H₂O (18 g, 99%, Aldrich) was dissolved in 20 g of distilled water. This solution was mixed with 20 g of the template and stirred at room temperature until all of the solution was adsorbed. After drying in an oven at 120 °C, this process (impregnation and drying) was repeated one additional time to obtain the SnO₂ precursor/SiO₂. The composite was further annealed at 400 °C for 3 h and the silica template was removed from the SnO₂/SiO₂ composite by treating with dilute 1 M NaOH solution for 30 min and washing with distilled water and ethanol several times. Finally, the powders were vacuum-dried at 120 °C overnight.

Characterization

For the electrochemical tests,¹⁴ the electrode for the battery test cells were made of the active material, super P carbon black, and polyvinylidene fluoride (PVDF) binder in a weight ratio of 8 : 1 : 1. The slurry prepared by thoroughly mixing a *N*-methyl-2-pyrrolidone (NMP) solution of PVDF, carbon black, and the cathode material was coated onto Cu foil with a thickness of 60 μm. The coated electrode was dried at 150 °C for 20 min and was roll-pressed. The coin-type half cells (2016 R-type) were prepared in a helium-filled glove box contained a electrode, a Li metal anode, a microporous polyethylene separator, and an electrolyte solution of 1 M LiPF₆ in ethylene carbonate–dimethyl carbonate (EC–DMC, 1 : 1 vol%). Each cathode contained ~25 mg of the SnO₂ material. There is a possibility that surface morphology of the Li anode may affect the rate capability of the cell. However, highly reproducible cycling results of both nanowire and mesoporous SnO₂ were obtained because same lithium metal and electrolytes were used for the cell assemblage.

The XRD patterns were obtained using Cu K α radiation at 10 kW. The nitrogen adsorption isotherm was measured at 77 K on a Micromeritics ASAP 2010 gas sorption system. Inductively coupled plasma-mass spectroscopy (ICP, ICPS-1000IV, Shimadzu) was used to determine the Na and Si contents of the final products.

Results and discussion

Fig. 1 shows low-angle XRD patterns of the nanowire and mesoporous SnO₂ after removing the SBA-15 and KIT-6 templates.

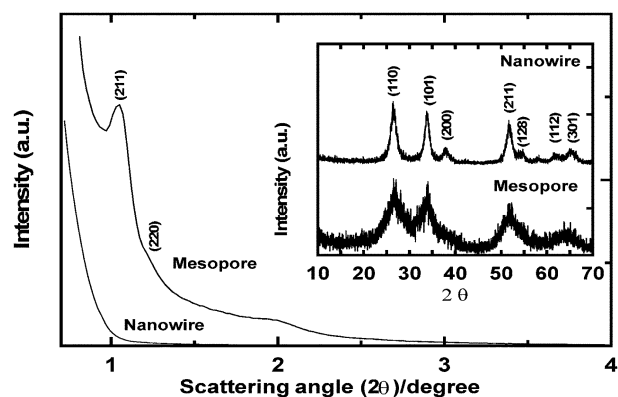


Fig. 1 Low-angle XRD patterns of mesoporous and nanowire SnO₂. High-angle X-ray diffraction patterns of mesoporous and nanowire SnO₂ are shown in the inset.

Low-angle XRD patterns, N₂ isotherms, and the pore size distribution of two mesoporous silica compounds, annealed SBA-15 and KIT-6 at 550 °C for 3 h, can be found in ESI† S1. The (211) diffraction peak confirms the formation of well-ordered *Ia3d* cubic mesoporous structure, and the unit cell constant (*a*) was estimated as 20.6 nm, which is smaller than that of the KIT-6 template (21.8 nm). The decreased unit cell constant is due to the shrinkage of mesoporous SnO₂ under thermal annealing at 400 °C. The high-angle XRD pattern in the inset of Fig. 1 indicates the formation of nanocrystalline SnO₂ with a tetragonal rutile structure (JCPDS 41-1445), which belongs to the space group *P4₂/mmm*. The average crystal domain size calculated from the peak broadening of the high-angle XRD pattern estimated using the Scherrer equation is approximately 3.2 nm ± 0.2 nm. On the other hand, SnO₂ nanowires do not show a peak in the low angle region in Fig. 1, which means that pore size distribution is not uniform in the nanowire bundles. The corresponding high-angle XRD pattern also confirms the formation of nanocrystalline SnO₂, but the peak widths decrease compared with those of mesoporous SnO₂. The average crystal domain size was estimated as 6.5 ± 0.2 nm. ICP-MS results of the mesoporous and hollow SnO₂ showed that residual Si from SiO₂ was 80 and 90 ppm, respectively, but residual Na from NaOH was not detected in either sample. High angle XRD patterns of the nanowire and mesoporous SnO₂ do not show the diffraction peaks of Na₂SnO₃ with major peaks at 39.2° and 16.2°, indicating that SnO₂ did not react with NaOH during etching.

The nanowire morphology of SnO₂ prepared from SBA-15 is shown in Fig. 2A and B. An individual nanowire has a diameter of about 6 nm and a length of >3 μm, as evidenced by the TEM (Fig. 2A) and SEM images (ESI† S2). In general, metal oxides prepared from a SBA-15 template lead to aggregated nanowires, and our nanowire morphology is quite similar to that of nanowire CeO₂.¹⁶ A high resolution TEM image (Fig. 2B) shows that the nanowires consist of nanocrystalline domains that are not structurally coherent, and that lattice fringes exist with *d* spacing values of 3.35 Å and 1.67 Å, corresponding to the (110) and (220) planes of SnO₂.

Fig. 2C and D shows TEM images of mesoporous SnO₂ formed from KIT-6 that has a cubic nanostructure which replicates the

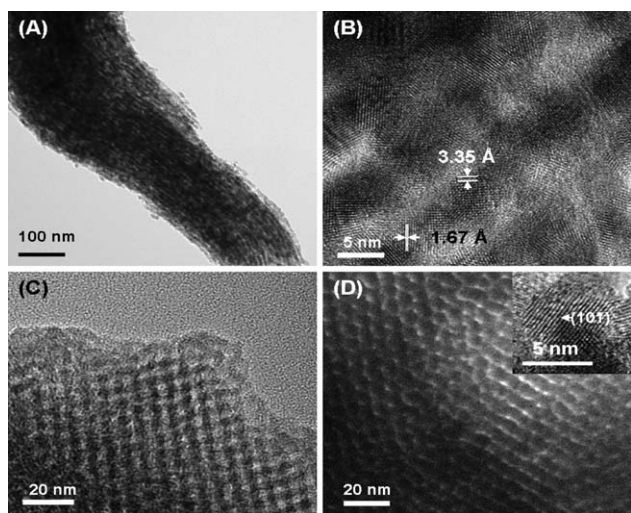


Fig. 2 TEM images of SnO₂ nanowires (A) along the [110] direction of the *p6mm* structure, (B) HRTEM image of (A). TEM images of mesoporous SnO₂ along the (C) [110] and (D) [100] directions.

pore structure of the template in which nearly all the SnO₂ is present in the form of a connected, mesostructured network. A high-resolution TEM image (inset of Fig. 2D) shows a lattice fringe with a distance of 2.64 Å, which is the (101) spacing of the SnO₂ structure. The diameter of the SnO₂ particles in Fig. 2C and D is ~5.2 nm, which is correlated to the channel diameter of the KIT-6 template. This value, however, is smaller than the KIT-6 channel diameter (~6.1 nm), which is due to the incomplete occupation of the pore space by SnO₂ after annealing at 400 °C. On the other hand, this smaller particle size can also be attributed to the contraction of the SnO₂ particles during the annealing process. Accordingly, the pore size of the mesoporous SnO₂ is slightly larger than the pore-wall thickness of the KIT template.

The nitrogen adsorption isotherms of the nanowire and mesoporous SnO₂ are shown in Fig. 3, showing BET surface areas of 80 and 160 m² g⁻¹, respectively. The measured surface area of mesoporous SnO₂ is higher than those of other mesoporous SnO₂ samples prepared by soft template routes. For instance, crystalline mesoporous SnO₂ prepared using a PB-PEO

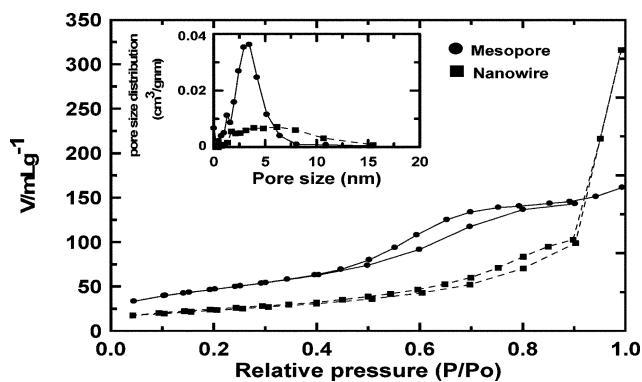


Fig. 3 Nitrogen adsorption and desorption isotherms for the mesoporous and nanowire SnO₂. The corresponding BJH distributions are shown in the inset.

structural directing agent in THF solvent achieved a pore size of 3.5 nm and a BET surface area of 60 m² g⁻¹.²¹ The nitrogen isotherm curve of the mesoporous SnO₂ has a well-defined step, which is characteristic of framework-confined mesopores. As shown in the inset of Fig. 3 the average pore size in the mesoporous sample is approximately 3.8 nm by a Barrett–Joyner–Halenda (BJH) analysis. The pore volume of mesoporous SnO₂ was 0.34 cm³ g⁻¹. The pore wall thickness of the starting cubic KIT-6 was estimated to be ~3 nm, and the pore size of mesoporous SnO₂ is larger than the pore-wall thickness of KIT-6 due to the incomplete occupation of the pore spaces by SnO₂. A similar result was observed in mesoporous carbon and Co₃O₄ from silica templates.^{15,17} A type IV adsorption–desorption isotherm with H2-type hysteresis was observed, and pronounced hysteresis was observed. This is characteristic of mesoporous ordered domains. The N₂ isotherm of nanowire SnO₂ shows the typical curve of a nanostructured material which does not have mesopores, and the pore size distribution is broad, showing that the pore size distribution is not uniform. This is also well supported by the low angle XRD pattern as described above.

Fig. 4 shows the cycle-life performance of the nanowire SnO₂ after 1, 10, 20, 30, 40, 50 cycles which cycled between 1.2 and 0 V at a rate of 0.2 C (= 400 mA g⁻¹). The first discharge and the charge capacity of the nanowires were 1400 and 795 mAh g⁻¹, respectively (the irreversible capacity ratio is 43%), and the

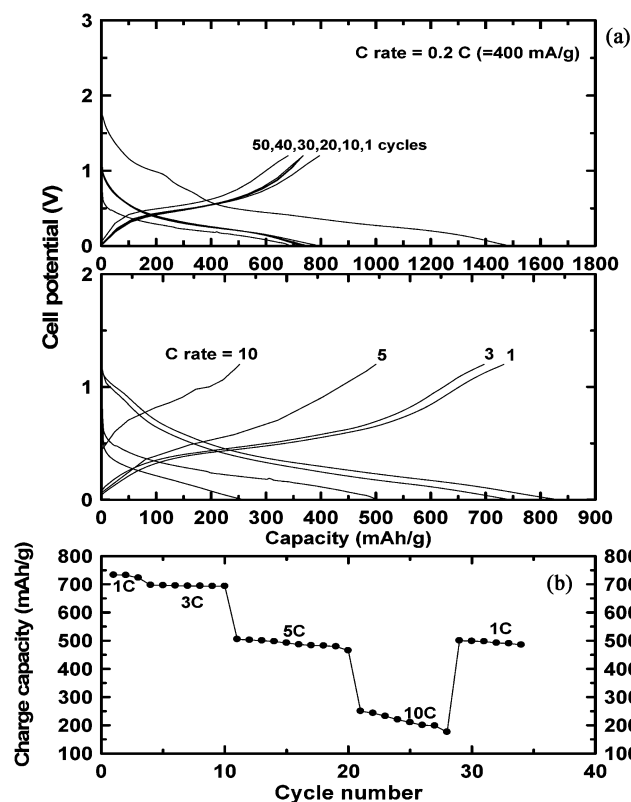


Fig. 4 (a) Voltage profiles of the nanowire SnO₂ anode in coin-type half-cells during the 1st, 5th, 10th, 20th, 30th, 40th and 50th cycles between 1.2 and 0 V. The discharge C rate was maintained at 0.2 C (= 400 mA g⁻¹). (b) Plot of the charge capacities of the nanowire SnO₂ anode vs. cycle number at different discharge rates of 1, 3, 5 and 10 C in coin-type half-cells. The discharge C rate was maintained at 0.2 C (= 400 mA g⁻¹).

capacity retention rate after 50 cycles is 85% at a rate of 0.2 C between 0 and 1.2 V. The high level of irreversible capacity during the first cycle is associated with the formation of an irreversible inactive Li_2O phase and possible side reactions with the electrolytes during the decomposition of SnO_2 ($\text{SnO}_2 + 4\text{Li}^+ + 4\text{e}^- \rightarrow \text{Li}_2\text{O} + \text{Sn}$).⁸

Compared with self-catalysis-grown SnO_2 nanowires which have about 100 nm diameter, that showed a capacity decrease from 910 mAh g^{-1} to 220 mAh g^{-1} at a current density of 100 mA g^{-1} after 50 cycles,¹¹ the capacity retention of the nanowires obtained from the template shows a significantly improved value (680 mAh g^{-1}). This improvement may be related to the spaces between the nanowires acting as buffer layers during the lithium reactions. On the other hand, Li *et al.* reported that nanostructured SnO_2 nanofiber electrodes like the bristles of a brush can be prepared *via* the polycarbonate template membrane.⁵ Since the construction of the electrode is completely different from this study and other studies,^{9–12,14} rate capabilities cannot directly be compared. However, SnO_2 nanofibers protruding from a Pt current collector showed capacity retention of 72% even at a rate of 30 C.

As the SnO_2 nanowires are aligned with different crystal orientations, an anisotropic volume change during the lithium alloy and dealloy processes can be expected. Although nanoscale materials can result in better capacity retention compared to micron-sized particles due to a more homogenous volume change and reduced absolute volume change between Sn and Li_xSn ,⁷ nanoparticles would nonetheless aggregate into larger particles, resulting in pulverization and electrical disconnection with the current collector. Accordingly, a 50 cycled electrode shows some fragmentation of the nanowires into aggregated nanoparticles $\sim 5 \text{ nm}$ in size, inducing a capacity decay (Fig. 5). A TEM image shows the formation of tetragonal Sn with different lattice fringes of (200) and (211), corresponding to 2.95 and 1.99 Å, respectively (Fig. 5).

When the cell is cycled at high rates from 1, 3, 5 and 10 C (with a discharge rate fixed at 0.2 C), the charge capacity decreases slowly out to 3 C, after which it decreases rapidly, showing 697, 500, and 250 mAh g^{-1} at 3, 5, and 10 C rates, respectively; the capacity retention at a 10 C rate, compared with 1 C, is 31%. In addition, capacity recovery after 8 cycles at 10 C rate is 68% of the capacity at 1 C rate. This result indicates that nanowires may undergo higher degrees of nanowire pulverization than those cycled at lower C rate.

On the other hand, mesoporous SnO_2 shows an increased irreversible capacity, although the charge capacity remains

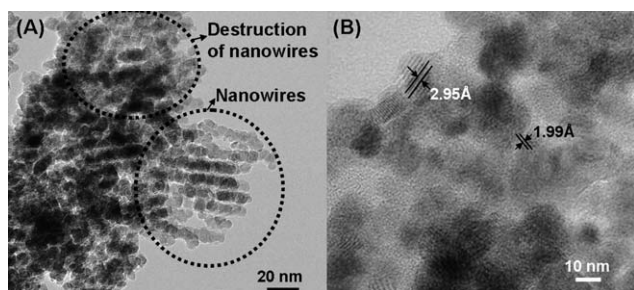


Fig. 5 (A) TEM image of the nanowire SnO_2 electrode after 50 cycles and (B) a high-resolution image of (A).

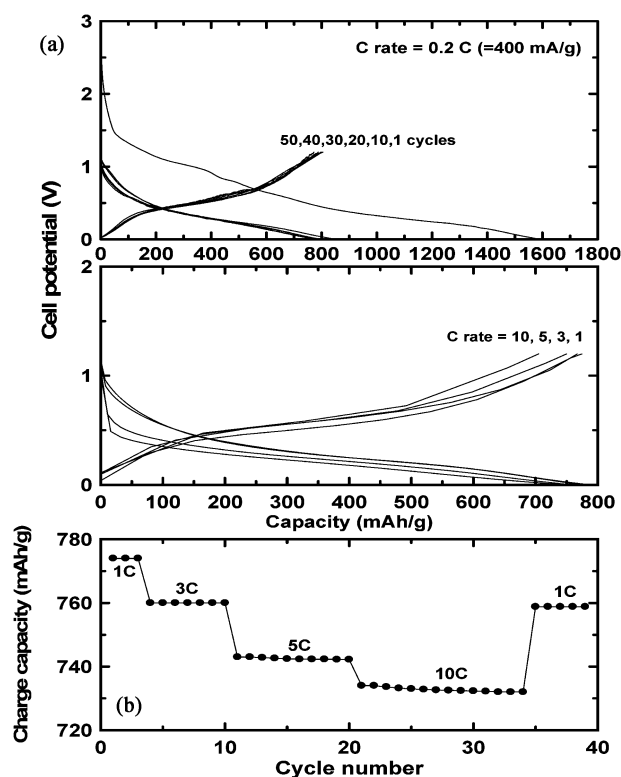


Fig. 6 (a) Voltage profiles of the mesoporous SnO_2 anode in coin-type half-cells during the 1st, 5th, 10th, 20th, 30th, 40th and 50th cycles between 1.2 and 0 V. The discharge C rate was maintained at 0.2 C (= 400 mA g^{-1}). (b) Plot of the charge capacities of the mesoporous SnO_2 anode vs. cycle number at different discharge rates of 1, 3, 5 and 10 C in coin-type half-cells. The discharge C rate was maintained at 0.2 C (= 400 mAh g^{-1}).

similar to that of the nanowires, showing initial discharge and charge capacities of 1595 mAh g^{-1} and 800 mAh g^{-1} , respectively, and an irreversible capacity ratio of 50% (Fig. 6). The capacity retention after 50 cycles is 773 mAh g^{-1} , showing a capacity retention ratio of 96%. Its capacity retention is improved by 11% compared with that of the nanowires. It is believed that this is due to the mesopores that act as a buffer zone against volume expansion of the SnO_2 wall frames. This is well supported by the TEM image (Fig. 7) of the cycled SnO_2 , and the pore size is estimated as $\sim 5 \text{ nm}$, which is similar to that of pristine SnO_2 . As the regular porosity with a higher surface to-volume ratio permits intimate flooding of the electrolytes

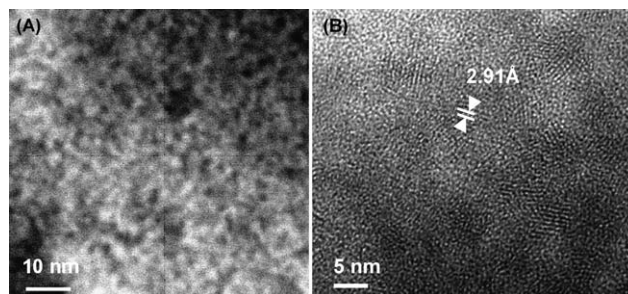


Fig. 7 TEM image of (A) the mesoporous SnO_2 electrode after 50 cycles and (B) a high-resolution image of (A).

between the particles, greatly enhanced rate capabilities can be expected. Fig. 6b and c show the cycling curves of mesoporous SnO₂ and capacity variations as the *C* rate increases from 1, 3, 5, to 10 *C*. The charge capacities are 775, 767, 743, and 734 mAh g⁻¹, respectively (the discharge rate was fixed at 0.2 *C*). In particular, the capacity retention at 10 *C* is improved by 70% compared with the nanowires. Moreover, the capacity after 10 *C* rate cycles is recovered to 760 mAh g⁻¹, corresponding to 98% of the capacity at a 1 *C* rate. Although there is no direct comparison with other nanoscale SnO₂ particles, it shows a comparable result to porous Cu–Sn alloys that were 73% at a 10 *C* rate.²²

Conclusions

Mesoporous and nanowire SnO₂ prepared using KIT-6 and SBA-15 hard templates led to facile and reproducible nanowire and mesoporous SnO₂. Mesoporous SnO₂ showed higher capacity retention than the nanowire counterpart due to the quicker Li⁺ ion diffusion through mesopores flooded with the electrolyte. However, a drawback of these SnO₂ was enhanced irreversible capacity due to their high BET surface areas, but their irreversible capacities are expected to be reduced by the inactive carbon coating.¹⁴ It should be noted that the inherent irreversible capacity contribution from Li₂O during the first alloy process cannot be overcome.

Acknowledgements

This research was financially supported by the Ministry of Commerce, Industry and Energy (MOCIE) and Korea Industrial Technology Foundation (KOTEF) through the Human Resource Training Project for Regional Innovation.

References

- 1 Z. Liu, D. Zhang, S. Han, C. Li, T. Tang, W. Jin, X. Liu, B. Lei and C. Zhou, *Adv. Mater.*, 2003, **15**, 1754.
- 2 Y. Liu, J. Dong and M. Liu, *Adv. Mater.*, 2004, **16**, 353.
- 3 Z. R. Dai, Z. W. Pan and Z. L. Wang, *J. Am. Chem. Soc.*, 2002, **124**, 8673.
- 4 J. Q. Hu, X. L. Ma, N. G. Shang, Z. Y. Xie, N. B. Wong, C. S. Lee and S. T. Lee, *J. Phys. Chem. B*, 2002, **106**, 3823.
- 5 N. Li, C. R. Martin and B. Scrosati, *Electrochem. Solid-State Lett.*, 2000, **3**, 316; N. Li and C. R. Martin, *J. Electrochem. Soc.*, 2001, **148**, A164.
- 6 Y. Idota, T. Kubota, A. Matsufuji, Y. Maekawa and T. Miyasaka, *Science*, 1997, **276**, 1395.
- 7 (a) I. A. Courtney and J. R. Dahn, *J. Electrochem. Soc.*, 1997, **144**, 2045; (b) I. A. Courtney, J. S. Tse, O. Mao, J. Hafner and J. R. Dahn, *Phys. Rev. B*, 1998, **58**, 15583.
- 8 C. Kim, M. Noh, M. Choi, J. Cho and B. Park, *Chem. Mater.*, 2005, **17**, 3297.
- 9 (a) Y. Wang and J. Y. Lee, *J. Phys. Chem. B*, 2004, **108**, 17832; (b) Y. Wang, H. C. Zeng and J. Y. Lee, *Adv. Mater.*, 2006, **18**, 645; (c) Y. Wang, J. Y. Lee and H. C. Zeng, *Chem. Mater.*, 2005, **17**, 3899.
- 10 (a) Y. Wang, F. Su, J. Y. Lee and X. S. Zhao, *Chem. Mater.*, 2006, **18**, 1347; (b) X. W. Lou, Y. Wang, C. Yuan, J. Y. Lee and L. A. Archer, *Adv. Mater.*, 2006, **18**, 2325; (c) S. Han, B. Jang, T. Kim, S. M. Oh and T. Hyeon, *Adv. Funct. Mater.*, 2005, **15**, 1845.
- 11 M.-S. Park, G.-X. Wang, Y.-M. Kang, D. Wexler, S.-X. Dou and H.-K. Liu, *Angew. Chem., Int. Ed.*, 2007, **46**, 750.
- 12 F. Chen and M. Liu, *Chem. Commun.*, 1999, 1829.
- 13 D.-F. Zhang, L.-D. Sun, J.-L. Yin and C.-H. Yan, *Adv. Mater.*, 2003, **12**, 1022.
- 14 (a) E. Kim, D. Son, T.-G. Kim, J. Cho, B. Park, K. S. Ryu and S. H. Chang, *Angew. Chem., Int. Ed.*, 2004, **43**, 5987; (b) E. Kim, M. G. Kim, Y. Kim and J. Cho, *Electrochem. Solid-State Lett.*, 2005, **8**, A452; (c) E. Kim, Y. Kim, M. G. Kim and J. Cho, *Electrochem. Solid-State Lett.*, 2006, **9**, A156; (d) H. Kim, G.-S. Park, E. Kim, S.-G. Doo and J. Cho, *J. Electrochem. Soc.*, 2006, **153**, A1633.
- 15 K. P. Gierszal, T.-W. Kim, R. Ryoo and M. Jaroniec, *J. Phys. Chem. B*, 2005, **109**, 8774.
- 16 S. C. Laha and R. Ryoo, *Chem. Commun.*, 2003, 2138.
- 17 (a) Y. Wang, C.-M. Yang, W. Schmidt, B. Spliethoff, E. Bill and F. Schüth, *Adv. Mater.*, 2005, **17**, 53; (b) A. Ruplecker, F. Kleitz, E.-L. Salabas and F. Schüth, *Chem. Mater.*, 2007, **19**, 485.
- 18 B. Tian, X. Liu, H. Yang, S. Xie, C. Yu, B. Yu and D. Zhao, *Adv. Mater.*, 2003, **15**, 1370.
- 19 F. Kleitz, S. H. Choi and R. Ryoo, *Chem. Commun.*, 2003, 2136.
- 20 (a) N. Ulagappan and C. N. R. Rao, *Chem. Commun.*, 1996, 1685; (b) K. G. Severin, T. M. Abdel-Fattah and T. J. Pinnavaia, *Chem. Commun.*, 1998, 1471.
- 21 J. Ba, J. Polleux, M. Antonietti and M. Niederberger, *Adv. Mater.*, 2005, **17**, 2509.
- 22 H.-C. Shin and M. Liu, *Adv. Funct. Mater.*, 2005, **15**, 582.